

The signature of supernova ejecta in the X-ray afterglow of the γ -ray burst 011211

J. N. Reeves*, D. Watson*, J. P. Osborne*, K. A. Pounds*, P. T. O'Brien*
 A. D. T. Short*, M. J. L. Turner*, M. G. Watson*, K. O. Mason†, M. Ehle‡
 & N. Schartel‡

*X-ray Astronomy Group, Department of Physics and Astronomy, University of Leicester, University Road, Leicester LE1 7RH, UK

†Mullard Space Science Laboratory, University College London, Holmbury St Mary, Dorking RH5 6NT, UK

‡XMM-Newton SOC, Villafranca, 28080, Madrid, Spain

Now that γ -ray bursts (GRBs) have been determined to lie at cosmological distances¹, their isotropic burst energies are estimated to be as high as 10^{54} erg (ref. 2), making them the most energetic phenomena in the Universe. The nature of the progenitors responsible for the bursts remains, however, elusive. The favoured models range from the merger of two neutron stars in a binary system^{3–5} to the collapse of a massive star^{6–8}. Spectroscopic studies of the afterglow emission could reveal details of the environment of the burst, by indicating the elements present, the speed of the outflow and an estimate of the temperature. Here we report an X-ray spectrum of the afterglow of GRB011211, which shows emission lines of magnesium, silicon, sulphur, argon, calcium and possibly nickel, arising in metal-enriched material

with an outflow velocity of the order of one-tenth the speed of light. These observations strongly favour models³⁰ where a supernova explosion from a massive stellar progenitor precedes the burst event and is responsible for the outflowing matter.

The γ -ray burst GRB011211 was first detected on 11 December 2001 at 19:09:21 UT, by the Beppo-SAX satellite⁹; the burst duration was 270 s (making GRB011211 the longest burst observed by Beppo-SAX), with a peak flux (40–700 keV) of 5×10^{-8} erg cm⁻² s⁻¹. Spectroscopy of the optical afterglow revealed several absorption lines at a redshift of $z = 2.141 \pm 0.001$ (refs 10, 11), and R-band imaging¹² has linked the optical transient with extended emission—the probable host galaxy—of magnitude $m_v = 25.0 \pm 0.5$. Assuming the absorption system arises from the GRB host galaxy, and adopting a cosmology of $H_0 = 75$ km s⁻¹ Mpc⁻¹ and $q_0 = 0.1$, implies a total equivalent isotropic energy for GRB011211 of 5×10^{52} erg.

The observations of GRB011211 by the orbiting XMM-Newton¹³ X-ray telescope started at 06:16:56 UT on 12 December 2001, 11 hours after the initial burst¹⁴. Data from the European Photon Imaging Cameras (EPIC) have been analysed, using both the MOS and PN instruments; the total observation duration is 27 ks. The time-averaged 0.2–10 keV flux, F , was 1.9×10^{-13} erg cm⁻² s⁻¹ (corresponding to a 0.6–30 keV rest-frame afterglow luminosity of 7×10^{45} erg s⁻¹), decreasing with time t during the observation as $F(t) \propto t^{-(1.7 \pm 0.2)}$. The Optical Monitor detected the burst afterglow in both the visible and ultraviolet (UVW1) bands (at 11σ and 6σ confidence), with magnitudes of 21.12 ± 0.13 and 21.6 ± 0.3 , respectively. The magnitudes correspond to fluxes of $(1.28 \pm 0.16) \times 10^{-17}$ erg cm⁻² s⁻¹ Å⁻¹ and $(0.85 \pm 0.23) \times 10^{-17}$ erg cm⁻² s⁻¹ Å⁻¹ at wavelengths of 5,430 Å and 3,140 Å,

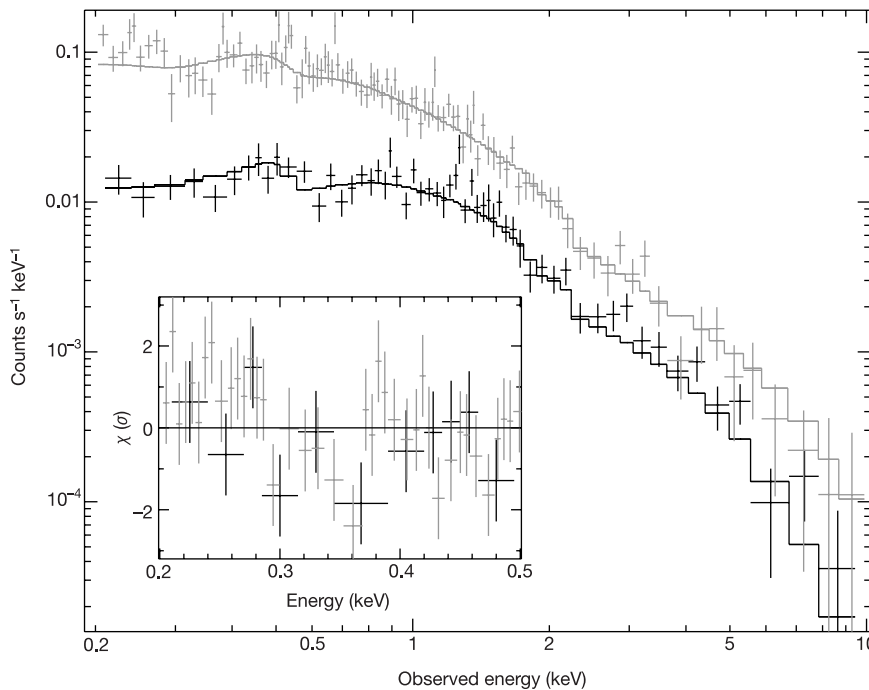


Figure 1 The XMM-Newton spectrum of the afterglow of the γ -ray burst, GRB011211. The spectrum shown is integrated over the whole 27-ks observation. EPIC-PN detector data points are shown in grey, EPIC-MOS detector points in black (see text). The ordinate shows the counts per second obtained in each detector, over a given energy range (keV), and the abscissa plots the observed energy (in the observed frame) of the X-ray photons. The solid curves show the model fit, convolved through the instrument response and energy resolution. In this case, the continuum emission can be modelled by either a power law of photon index $\Gamma = 2.3 \pm 0.1$ or thermal bremsstrahlung emission of temperature $kT = 2.1 \pm 0.2$ keV, attenuated only by an absorption column of 4.2×10^{20} cm⁻² from

our own Galaxy. An apparent absorption feature is present between 0.3 and 0.4 keV (see inset); this can be modelled by an absorption edge (where the opacity after the edge energy E_0 falls as E^{-3}). In the burst rest frame, the edge energy is $E_0 = 0.99 \pm 0.09$ keV with an optical depth $\tau = 1.0 \pm 0.4$. Assuming the above absorption feature arises in the same material as the line emission, then its likely identification is with the O VIII edge at 0.87 keV. Note however that although the absorption edge is formally significant (99.9% from an F -test), the detector resolution is lowest at this energy ($\Delta E \approx 100$ eV at 300 eV), which makes the shape of the feature difficult to constrain.

respectively. These data are consistent with reddening in the host galaxy of $E(B - V) \approx 0.2$, or with Lyman α absorption at high redshift. Figure 1 shows the time-averaged EPIC X-ray spectrum of the burst afterglow. The continuum can be fitted by a power law of photon index $\Gamma = 2.3 \pm 0.1$, attenuated by the Galactic absorption column of $4.2 \times 10^{20} \text{ cm}^{-2}$. An apparent absorption feature is present between 0.3 and 0.4 keV, which, when fitted by an absorption edge, gives an energy of $E_0 = 0.99 \pm 0.09 \text{ keV}$ and an optical depth of $\tau = 1.0 \pm 0.4$, in the burst rest frame.

Spectra were initially extracted in five time segments, corresponding to 0–5 ks, 5–10 ks, 10–15 ks, 15–20 ks and 20–27 ks after the start of the XMM-Newton observation. As significant line emission was observed only during the initial 10 ks, the remaining data were binned into one 17-ks time bin. Figure 2 shows the EPIC-PN spectrum between 0.2 and 3 keV, from the first 5 ks only; emission lines are detected in the burst rest frame at energies (keV) of 1.40 ± 0.05 , 2.19 ± 0.04 , 2.81 ± 0.04 , 3.79 ± 0.07 and 4.51 ± 0.12 . The closest abundant $K\alpha$ transitions to the observed lines are: Mg XI (1.35 keV) or Mg XII (1.47 keV), Si XIV (2.00 keV), S XVI (2.62 keV), Ar XVIII (3.32 keV) and Ca XX (4.10 keV). Thus we infer that the lines are blueshifted with respect to the known redshift of GRB011211. To quantify this, we adopted the rest-frame energies corresponding to Mg XI, Si XIV, S XVI, Ar XVIII and Ca XX, and varied the redshift of the line-emitting material. The best-fit redshift for the line set was found to be $z = 1.88 \pm 0.06$, differing significantly (at >99.99% confidence) from the known GRB redshift of $z = 2.140 \pm 0.001$, implying an outflow velocity (v) for the line emitting material of $v/c = 0.086 \pm 0.004$, where c is the velocity of light, or $v = 25,800 \pm 1,200 \text{ km s}^{-1}$. The line emission also declines

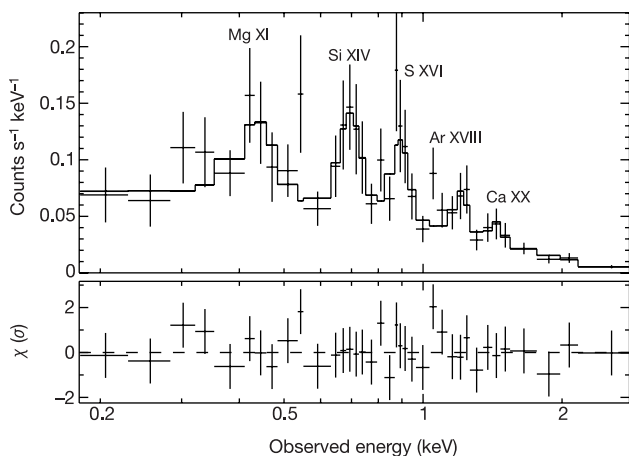


Figure 2 The XMM-Newton EPIC-PN spectrum of the burst afterglow, for the first 5 ks of exposure only. Top, the observed count rate spectrum; bottom, the residuals of the thermal model compared with the data points, in units of 1σ deviations. The energy plotted on the abscissa is in the observer frame. Emission lines are detected at energies (keV) of 0.45 ± 0.03 , 0.70 ± 0.02 , 0.89 ± 0.01 , 1.21 ± 0.02 and 1.44 ± 0.04 in the observed spectrum, whilst the measured line fluxes ($\text{erg cm}^{-2} \text{ s}^{-1}$) are $(7.6 \pm 5.1) \times 10^{-15}$, $(1.1 \pm 0.3) \times 10^{-14}$, $(9.9 \pm 2.9) \times 10^{-15}$, $(6.7 \pm 2.5) \times 10^{-15}$ and $(4.4 \pm 2.2) \times 10^{-15}$, respectively. These correspond to energies (keV) of 1.40 ± 0.05 , 2.19 ± 0.04 , 2.81 ± 0.04 , 3.79 ± 0.07 and 4.51 ± 0.12 in the burst rest frame (at $z = 2.14$), with rest-frame equivalent widths (eV) of 180 ± 120 , 430 ± 130 , 480 ± 140 , 460 ± 170 and 360 ± 180 , respectively (all errors are quoted at 1σ confidence). Note that an iron K line is not detected; the upper limit on the rest-frame equivalent width is $<400 \text{ eV}$. For reference, the resolution (full-width at half-maximum) of the EPIC-PN spectrum is 100 eV at 1 keV . The emission lines can be identified with the $K\alpha$ transitions of Mg XI (or Mg XII), Si XIV, S XVI, Ar XVIII, and Ca XX. The observed energies are blue-shifted by a factor corresponding to a velocity of $v = 0.086c$ (or $25,800 \text{ km s}^{-1}$), when compared to the redshift of the γ -ray burst (at $z = 2.14$). For clarity, only the EPIC-PN data are shown; consistent results are obtained for the EPIC-MOS camera, although the signal-to noise ratio of the MOS data is lower.

more rapidly than the continuum (at $>3\sigma$ confidence), suggesting a more enduring (non-thermal) component to the continuum flux. The decrease in flux of the Si XIV line is shown in Fig. 3; the line is detected only over the first 10 ks of observation.

In order to assess the quality of the spectral fit and the statistical significance of the emission lines, we calculated the fit statistic, measured in terms of total χ^2 deviations between the data points and the input model, divided by the degrees of freedom (d.o.f) in the fit. This improved from $\chi^2/\text{d.o.f} = 56.7/47$ for a pure power-law model to $36.2/41$ on the addition of the lines. Employing an F -test¹⁵ then yields a significance level of 99.7% for the set of lines as a whole. Furthermore, by performing Monte Carlo simulations, we find a probability of only 0.02% that the lines result from purely random Poisson noise. We conclude that the line emission is detected with good confidence.

X-ray line emission can arise by a variety of processes, including thermal emission, recombination in a photoionized plasma, or by reflection of hard X-rays in dense, optically thick matter. Modelling the early spectrum with emission from an optically thin plasma of temperature $kT = 4.5 \pm 0.5 \text{ keV}$ and luminosity $7 \times 10^{45} \text{ erg s}^{-1}$ (using the ‘MEKAL’ code¹⁶), requires an over-abundance for Mg, Si, S, Ar and Ca of about 10 times the solar value (solar abundance is ruled out at $>99.9\%$ confidence). The absence of emission in the Fe K band gives a limit to the abundance of iron at <1.3 times the solar value. The fit statistic for the thermal model is excellent ($\chi^2/\text{d.o.f} = 37/44$), and Monte Carlo simulations showed that only one in 10,000 pure power-law spectra could yield as good a fit by chance alone (that is, a null probability of about 0.01%). Another possible source of the line emission is X-ray reflection^{17,18}. This is currently favoured in ‘nearby reprocessor’ models¹⁹, where X-rays scatter off dense material within the stellar envelope of a massive progenitor star. We fitted ionized reflection models¹⁷ to the data for two cases: (1) where the walls of the stellar envelope subtend $2\pi \text{ sr}$ solid angle to the X-ray source; (2) where the emission arises purely from the scattered X-ray flux, with no continuum emission. In both cases the fit obtained is poor ($\chi^2/\text{d.o.f} = 62.4/46$ and $56.7/47$, respectively);

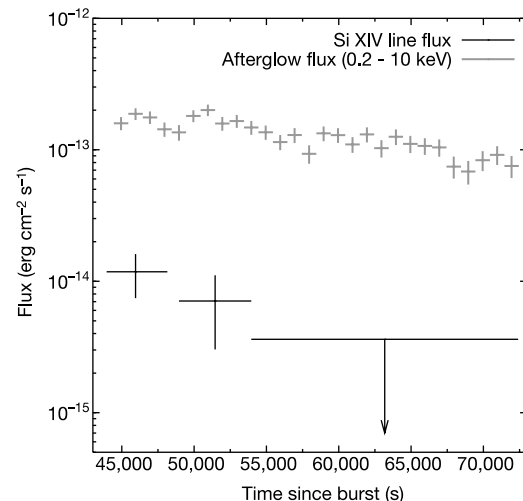


Figure 3 The line flux of Si XIV $K\alpha$, and the total continuum flux (0.2–10 keV), as a function of time since the initial burst. The Si XIV line is detected in the first 10 ks of the observation (illustrated by the first two data points), but is not detected during the remainder of the observation (the upper limit shown is at the 3σ confidence level). The values of the Si XIV line flux are $(1.1 \pm 0.3) \times 10^{-14} \text{ erg cm}^{-2} \text{ s}^{-1}$ during the first 5 ks, $(0.7 \pm 0.4) \times 10^{-14} \text{ erg cm}^{-2} \text{ s}^{-1}$ from 5 to 10 ks and $<3.6 \times 10^{-15} \text{ erg cm}^{-2} \text{ s}^{-1}$ during the last 17 ks of observation. A similar effect is seen for the other emission lines, none being detected in the later part of the observation. For instance, the S XVI line flux is $(1.0 \pm 0.3) \times 10^{-14} \text{ erg cm}^{-2} \text{ s}^{-1}$ in the first 5 ks, decreasing to $<2.5 \times 10^{-15} \text{ erg cm}^{-2} \text{ s}^{-1}$ during the last 17 ks of observation.

the reflection models fail to reproduce the emission lines observed in the early afterglow spectrum.

A major drawback of both the photoionization and reflection models is that they favour emission from heavier metals such as Fe or Ni, rather than the lighter elements (because the line fluxes increase as the square of the atomic number), which is difficult to reconcile with the observed line spectrum. Therefore we consider the thermal model to be physically plausible, noting that the non-detection of Fe line emission is then a less severe constraint. We assume that a dense shell of material (the ejecta of a very recent supernova) is heated by the γ -ray burst. At the densities deduced below, the emitting plasma will rapidly reach thermal equilibrium, and will radiate over a timescale given by $t_{\text{cool}} \approx 2 \times 10^{15} n_e^{-1} T_8^{1/2}$ s, where T_8 is the plasma temperature in units of 10^8 K, and n_e is the electron density (in cm^{-3}). From the observed X-ray luminosity, we estimate an emission measure $n_e^2 V = 10^{69} \text{cm}^{-3}$, where V is the total emitting volume, whilst the temperature is also derived from the thermal spectrum (4.5 keV or 5×10^7 K). We interpret the observed emission line timescale (t) in terms of the light travel delay in radiation arising from different parts of the illuminated shell. For a spherical shell this delay depends on the radius of the shell R and the beam half-opening angle θ , and is given by $R = ct / (1 - \cos \theta)$. Converting the duration of the line emission to the burst rest-frame, $t = 10^4 / (1+z)$ s, for a half-opening angle of $\theta \approx 20^\circ$ (consistent with GRB beaming models²⁰), yields $R \approx 10^{15}$ cm. Combining the emission measure of illuminated matter, with an electron scattering optical depth of approximately 1 for the shell, then allows estimates (for $R \approx 10^{15}$ cm) of the electron density $n_e \approx 10^{15} \text{cm}^{-3}$ and shell thickness $\sim 10^9$ cm (in practice the ejecta may be clumpy, and thus distributed over a thicker shell). The mass of the illuminated matter is then approximately 0.1 solar masses ($\sim 10^{32}$ g) with a kinetic energy of $\sim 10^{51}$ erg, consistent with the energies of a typical supernova and the γ -ray burst (if beamed). In the isotropic limit, where the thermal emission results from a spherical shell of solid angle 4π sr, then the radius of the shell will simply be $R = ct$, yielding $R \approx 10^{14}$ cm; this sets a minimum distance between the burst and the line-emitting material. We might also expect to see redshifted line emission from the counter-jet receding from us, but matter outside the beam may prevent the X-ray emission from the far side of the shell being seen.

With a mean outflow velocity of the ejecta of 0.1c, the estimated radius of the shell, $R \sim 10^{15}$ cm, implies a time delay between the supernova and γ -ray burst of about 4 days (in the isotropic limit, this time delay will be a minimum of 10 hours). This offers a natural explanation for the non-detection of Fe K emission in the XMM-Newton spectrum. The stable isotope ^{56}Fe is produced by β -decay via the reaction $^{56}\text{Ni} \rightarrow ^{56}\text{Co} \rightarrow ^{56}\text{Fe}$, the reactions having half-lives of 6 and 78 days, respectively. Over a short timescale after the supernova, as our model implies, very little Fe will have been synthesized. Instead, we would expect to observe spectral features due to Ni or Co. We note that we do find a marginal detection (90% confidence) of the blueshifted Ni K α emission line, with a rest-frame equivalent width of 800 eV (equivalent to an eventual iron abundance of four times the solar value). Although iron will be present in the collapsed core of the massive progenitor, most of the illuminated ejecta will be from the outer stellar layers (that is, the lower-atomic-number elements). Our result contrasts with the large masses of iron implied by the iron lines reported in the X-ray spectra of several other afterglows^{21–23}. It seems plausible that in some of those cases, the actual detection was of Ni K α ²⁴; otherwise a much longer delay between an initial supernova and the onset of the γ -ray burst is required, of the order of several months.

The XMM-Newton observations reported here seem to rule out a neutron-star binary merger as the progenitor of GRB011211, as such a merger is unlikely to expel sufficient quantities of matter into the surrounding medium²⁵, nor can the relatively low iron abun-

dance be explained, as any supernova will have occurred many years before the stellar merger. The X-ray-emitting plasma has a high density, over-abundant light metals, and a high velocity outflow—this combination of properties strongly suggests an association of GRB011211 with a very recent supernova, caused by the collapse of a massive progenitor star²⁶. In this model, the supernova ejects a substantial quantity of enriched material at high velocity ($\sim 0.1c$) into the surrounding medium, which is subsequently illuminated by the γ -ray burst. The high metal abundances of the illuminated material would arise naturally from the pre-supernova nucleosynthesis and the short interval between the supernova explosion and the burst itself. Indeed, the supernova model is theoretically preferred over neutron-star mergers as the explanation of long-duration γ -ray bursts⁷, as seen here. The supernova link is further strengthened by the observed correlation of long-duration bursts with star-forming regions^{27,28}, and, in one case, a direct association between the bright supernova 1998bw and the very-low-redshift ($z = 0.0086$) γ -ray burst, GRB980425²⁹.

Received 21 January; accepted 6 March 2002.

1. Metzger, M. R. *et al.* Spectral constraints on the redshift of the optical counterpart to the γ -ray burst of 8 May 1997. *Nature* **387**, 878–880 (1997).
2. Meszaros, P. Theories of gamma-ray bursts. Preprint astro-ph/0111170 at (<http://xxx.lanl.gov>) (2001).
3. Paczynski, B. Gamma-ray bursters at cosmological distances. *Astrophys. J.* **308**, L43–L46 (1986).
4. Eichler, D., Livio, M., Piran, T. & Schramm, D. N. Nucleosynthesis, neutrino bursts and γ -rays from coalescing neutron stars. *Nature* **340**, 126–128 (1989).
5. Mochkovich, R., Hernanz, M., Isern, J. & Martin, X. Gamma-ray bursts as collimated jets from neutron star/black hole mergers. *Nature* **361**, 236–238 (1993).
6. Woosley, S. E. Gamma-ray bursts from stellar mass accretion disks around black holes. *Astrophys. J.* **405**, 273–277 (1993).
7. Paczynski, B. Are gamma ray bursts in star-forming regions? *Astrophys. J.* **494**, L45–L48 (1998).
8. Fryer, C. L., Woosley, S. E. & Hartmann, D. H. Formation rates of black hole accretion disk gamma-ray bursts. *Astrophys. J.* **526**, 152–177 (1999).
9. Frontera, F. *et al.* GRB011211: BeppoSAX/GRBM data. *GCN GRB Obs. Rep. No. 1215* (2001).
10. Fruchter, A. *et al.* GRB 011211: Spectroscopy of the optical counterpart. *GCN GRB Obs. Rep. No. 1200* (2001).
11. Holland, S. *et al.* The optical afterglow of the gamma-ray burst GRB 011211. *Astron. J.* (submitted); preprint astro-ph/0202309 at (<http://xxx.lanl.gov>) (2002).
12. Burud, I. *et al.* GRB 011211: Detection of the probable host galaxy. *GCN GRB Obs. Rep. No. 1213* (2001).
13. Jansen, F. *et al.* XMM-Newton observatory. I. The spacecraft and operations. *Astron. Astrophys.* **365**, L1–L6 (2001).
14. Santos-Lleo, M., Loiseau, N., Rodriguez, P., Altieri, B. & Schartel, N. GRB 011211: XMM-Newton observation of GRB011211. *GCN GRB Obs. Rep. No. 1192* (2001).
15. Bevington, P. R. & Robinson, D. K. *Data Reduction and Error Analysis for the Physical Sciences* (McGraw-Hill, New York, 1992).
16. Mewe, R., Gronenschild, E. H. B. M. & van den Oord, G. H. J. Calculated X-radiation from optically thin plasmas. *Astron. Astrophys. Suppl.* **62**, 197–254 (1985).
17. Ballantyne, D. R. & Ramirez-Ruiz, E. Iron K α emission from X-ray reflection: Predictions for gamma-ray burst models. *Astrophys. J.* **559**, L83–L87 (2001).
18. Kallman, T. R., Meszaros, P., Rees, M. J. Iron K lines from gamma ray bursts. *Astrophys. J.* (submitted); preprint astro-ph/0110654 at (<http://xxx.lanl.gov>) (2002).
19. Rees, M. J. & Meszaros, P. Fe K α emission from a decaying magnetar model of gamma-ray bursts. *Astrophys. J.* **545**, L73–L75 (2000).
20. Frail, D. A. *et al.* Beaming in gamma-ray bursts: Evidence for a standard energy reservoir. *Astrophys. J.* **562**, L55–L58 (2001).
21. Piro, L. *et al.* Observation of X-ray lines from a gamma-ray burst (GRB991216): Evidence of moving ejecta from the progenitor. *Science* **290**, 955–958 (2000).
22. Antonelli, L. A. *et al.* Discovery of a redshifted iron K line in the X-ray afterglow of GRB 000214. *Astrophys. J.* **545**, L39–L42 (2000).
23. Piro, L. *et al.* Iron line signatures in X-ray afterglows of GRB by BeppoSAX. *Astron. Astrophys. Suppl.* **138**, 431–432 (1999).
24. McLaughlin, G. C., Wijers, R. A. M. J., Brown, G. E. & Bethe, H. A. Broad and shifted iron-group emission lines in gamma-ray bursts as tests of the hypernova scenario. *Astrophys. J.* (submitted); preprint astro-ph/0110614 at (<http://xxx.lanl.gov>) (2001).
25. Weth, C., Meszaros, P., Kallman, T. & Rees, M. J. Early X-ray/ultraviolet line signatures of gamma-ray burst progenitors and hypernovae. *Astrophys. J.* **534**, 581–586 (2000).
26. Wheeler, J. C., Yi, I., Hoeflich, P. & Wang, L. Asymmetric supernovae, pulsars, magnetars, and gamma-ray bursts. *Astrophys. J.* **537**, 810–823 (2000).
27. Bulik, T., Belczynski, K. & Zbijewski, W. Distribution of compact object mergers around galaxies. *Mon. Not. R. Astron. Soc.* **309**, 629–635 (1999).
28. Hanlon, L. *et al.* ISO detection of a 60 μm source near GRB 970508. *Astron. Astrophys.* **359**, 941–947 (2000).
29. Bloom, J. S. *et al.* The unusual afterglow of the γ -ray burst of 26 March 1998 as evidence for a supernova connection. *Nature* **401**, 453–456 (1999).
30. Vietri, M. & Stella, L. Supranova Events from Spin-up Neutron Stars: An Explosion in Search of an Observation. *Astrophys. J.* **527**, L43–L46 (1999).

Acknowledgements

This work is based on observations obtained with XMM-Newton, an ESA science mission with instruments and contributions directly funded by ESA Member States and the USA (NASA). We thank M. Rees, M. Davies, B. McBreen, R. Willingale and M. Barstow for critical reading of the manuscript, and for discussions.

Competing interests statement

The authors declare that they have no competing financial interests..

Correspondence and requests for materials should be addressed to J.N.R. (e-mail: jnr@star.le.ac.uk).

Bunching of fractionally charged quasiparticles tunnelling through high-potential barriers

E. Comforti, Y. C. Chung, M. Heiblum, V. Umansky & D. Mahalu

Braun Center for Submicron Research, Department of Condensed Matter Physics, Weizmann Institute of Science, Rehovot 76100, Israel

Shot noise measurements have been used to measure the charge of quasiparticles in the fractional quantum Hall (FQH) regime^{1–3}. To induce shot noise in an otherwise noiseless current of quasiparticles, a barrier is placed in its path to cause weak backscattering. The measured shot noise is proportional to the charge of the quasiparticles; for example, at filling factor $\nu = 1/3$, noise corresponding to $q = e/3$ appears. For increasingly opaque barriers, the measured charge increases monotonically, approaching $q = e$ asymptotically^{4,5}. It was therefore believed that only electrons, or alternatively, three bunched quasiparticles, can tunnel through high-potential barriers encountered by a noiseless current of quasiparticles. Here we investigate the interaction of $e/3$ quasiparticles with a strong barrier in FQH samples and find that bunching of quasiparticles in the strong backscattering limit depends on the average dilution of the quasiparticle current. For a very dilute current, bunching ceases altogether and the transferred charge approaches $q = e/3$. This surprising result demonstrates that quasiparticles can tunnel individually through high-potential barriers originally thought to be opaque for them.

In 1918, Schottky determined the charge of the electron by measuring the average square of the current fluctuations, $S = \langle i^2 \rangle$, resulting from the stochastic emission of electrons in a vacuum tube—naming it ‘shot noise’⁶. His expression $S = 2qI$ is a result of independent random events obeying Poisson distribution. Here, S is the spectral density of the fluctuations (in units of $A^2 Hz^{-1}$), q is the charge of the particle and I is the average current. Similar experiments were implemented^{1–3} in the FQH regime⁷, verifying the existence of fractionally charged quasiparticles⁸. A partially transmitting constriction, a quantum point contact (QPC), served in these experiments as an adjustable potential barrier in the path of the current, thus partitioning the transmitted charges. This random process is described by a binomial distribution, resulting in $S = 2qI(1 - t)$ at zero temperature, with $t \in [0, 1]$ being the transmission coefficient of the QPC^{4,9,10}. In the weak backscattering regime, the quasiparticles were found to traverse the QPC independently of each other and the measured charge was $q = e/3$ at filling factor $\nu = 1/3$ and $q = e/5$ for $\nu = 2/5$ (refs 1,2,3). As backscattering gets stronger, the tunnelling of individual quasiparticles becomes correlated, and in the limit of a pinched QPC and

$\nu = 1/3$ three quasiparticles were found to group together to tunnel through the barrier. Obviously, Schottky’s formula is inapplicable for correlated (or bunched) quasiparticles, but it can still be used to characterize the system with the effect of bunching being incorporated into an effective charge $q(t)$. Hence, the noise for a pinched QPC becomes electronic-like⁴, that is, with an effective charge of $q = e$. Moreover, a nearly universal behaviour was found for the evolution of the effective charge $q(t)$ (ref. 5), starting at $q(\text{openQPC}) = e/3$ and monotonically increases toward $q(\text{pinchedQPC}) = e$.

Here we explore the bunching properties of a pinched QPC when a sparse beam of $e/3$ quasiparticles impinges upon it. In other words, when there are not enough quasiparticles in close proximity to bunch into an ‘electron’, we may ask the following questions: (1) will

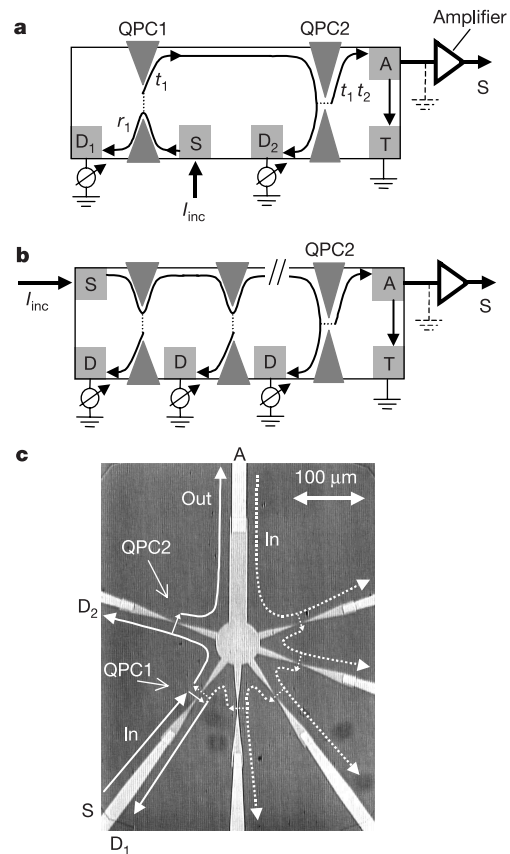


Figure 1 Schematic and actual representations of the quasiparticle injector followed by a quasiparticle filter, both made of quantum point contacts, QPC1 and QPC2, respectively. **a**, An injector made of a relatively open QPC1 partitions an incident noiseless (d.c.) current, injected from source terminal S. The scattered part (t_1), composed of a dilute beam of quasiparticles, impinges on a pinched QPC2. The resulting noise is measured by a cooled, low-noise, amplifier at terminal A (see ref. 1). The intermediate drain D_2 prohibits multiple reflections, and the grounded terminal T is used to fix the output impedance of the sample and make it independent of QPC settings. **b**, An alternative scheme, suitable for producing a moderately dilute current, invokes a cascade of weakly backscattering QPCs transmitting a dilute quasiparticle beam (see ref. 11). **c**, A photograph of the actual device in the vicinity of the QPCs, formed by metallic gates (light grey regions) deposited on the surface of the GaAs–AlGaAs heterostructure, embedding a two-dimensional electron gas some $0.1 \mu\text{m}$ below the surface. Electron mobility is $2 \times 10^6 \text{ cm}^2 \text{ V}^{-1} \text{ s}^{-1}$ and areal carrier density is $1.1 \times 10^{11} \text{ cm}^{-2}$, both measured at 4.2 K in the dark. The solid arrows correspond to the direction of current in configuration **a**, and the other QPCs on the right (with current flow denoted by dotted arrows) are used when configuration **b** is employed. Ohmic contacts (serving as S, D, T, A) are outside the frame of the picture.